Tada *et al. Earth, Planets and Space* (2024) 76:130
https://doi.org/10.1186/s40623-024-02063-y

Earth, Planets and Space

FULL PAPER

Open Access

Development of three-dimensional forward modeling method for the magnetometric resistivity (MMR) method

Noriko Tada[1*], Motoyuki Kido[2] and Nobukazu Seama[3]

Abstract

We have developed a 3-D forward modeling method for the magnetometric resistivity (MMR) technique, specially focusing on the marine MMR method, which utilizes a vertical bipole source and seafloor receivers to measure magnetic field variations. The bipole source generates an artificial electric current between two electrodes: one on the sea surface and another on the seafloor. When computing the electric potential using the relaxation method, while conserving electric current, singularities arise at the electrode locations. To address this issue, we introduce two electrical resistivity structures to mitigate the effects of these singularities and to obtain magnetic field anomalies caused by arbitrary 3-D electrical resistivity anomalies beneath the seafloor. By determining the sign of the magnetic field anomaly, we can infer whether the electrical resistivity of the anomalous body is more conductive or more resistive compared to the surrounding oceanic crust. Furthermore, we demonstrate that increasing the number of bipole sources is more effective in exploring anomalous bodies than increasing the number of receivers.

Keywords Controlled source electromagnetic methods, Magnetometric resistivity (MMR) method, 3-D forward modeling method, Electrical resistivity structure of oceanic crust, Singularity problem

*Correspondence:
Noriko Tada
norikot@jamstec.go.jp
Full list of author information is available at the end of the article

© The Author(s) 2024. **Open Access** This article is licensed under a Creative Commons Attribution 4.0 International License, which permits use, sharing, adaptation, distribution and reproduction in any medium or format, as long as you give appropriate credit to the original author(s) and the source, provide a link to the Creative Commons licence, and indicate if changes were made. The images or other third party material in this article are included in the article's Creative Commons licence, unless indicated otherwise in a credit line to the material. If material is not included in the article's Creative Commons licence and your intended use is not permitted by statutory regulation or exceeds the permitted use, you will need to obtain permission directly from the copyright holder. To view a copy of this licence, visit http://creativecommons.org/licenses/by/4.0/.

Graphical abstract

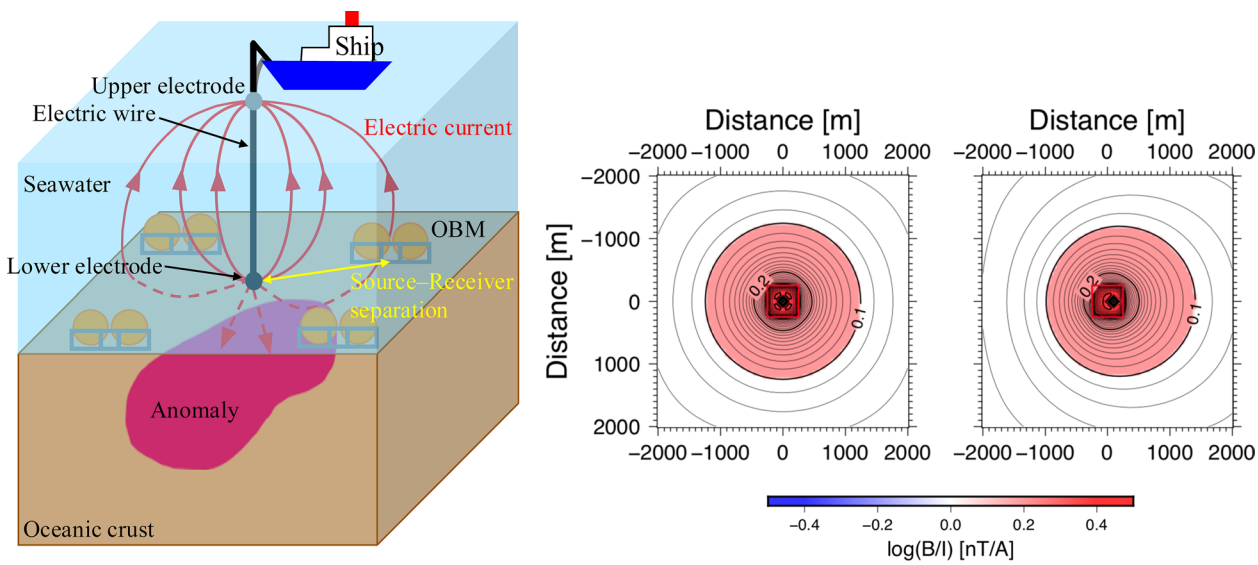

1 Introduction

Controlled source electromagnetic method (CSEM) is a non-destructive geophysical exploration technique that can reveal the electrical resistivity structure of shallow oceanic crust. The electrical resistivity (equal to the reciprocal of the electrical conductivity) is an important geophysical property independent of seismic velocity and gravity. Because the electrical resistivity is sensitive to the amount of fluid (seawater) and its distribution, temperature, and salinity, the electrical resistivity within shallow oceanic crust mainly depends on the ratio (porosity) and connectivity of rocks and fluids and their temperature. Thus, the electrical resistivity is a useful tool for understanding the distribution of fluids within the crust (e.g., hydrothermal circulation and underwater springs). CSEMs use artificial electric current as the source and induced magnetic and/or electric fields as response signals. Higher frequency signals generally yield shallower information about the electrical resistivity beneath the seafloor. In the ocean, high frequency signals decay or fade away while passing through seawater because of its high conductivity, and geomagnetic fields observed at the seafloor lack information about shallower structures. Thus, artificial sources are necessary for estimating the electrical resistivity of shallow oceanic crust.

Since the 2000s, CSEM methods have been actively conducted to research the electrical resistivity structures of shallow marine environments. For instance, Naif et al. (2015, 2016) conducted extensive observations perpendicular to the Middle America Trench to estimate fluid volumes in the oceanic crust near subduction zones, deriving porosity distributions from electrical resistivity values. Concurrently, resource explorations have been carried out for gas hydrates, with resistivities ranging from 10 Ω-m and above (Schwalenberg et al. 2010) to 1.8–3.5 Ω-m (Chesley et al. 2023), and for massive sulfides, with resistivities ranging from 0.1 to 0.4 Ω-m (Ishizu et al. 2024), all within shallow marine sediments with resistivities ranging from 0.8 to 3.5 Ω-m. More recently, integrated marine and terrestrial CSEM surveys and data analyses have been advanced around Martinique Island (Védrine et al. 2023).

The magnetometric resistivity (MMR) method is one of the techniques used in CSEM surveys, whose theory was first introduced by Edwards et al. (1978). The marine MMR method, as illustrated in Fig. 1, consists of two parts: a source and receivers. The source, called a "bipole source", is composed of two electrodes connected by electric wires to make an artificial bipole electric current that runs between one electrode on the sea surface and the other on the seafloor. The receivers are ocean bottom magnetometers (OBMs) deployed on the seafloor, which measure three components of magnetic field variations including the magnetic field induced by the bipole source. An advantage of the MMR method is its very simple operation in contrast to most CSEM methods that use horizontal sources (e.g., Constable and Weiss 2006). In the MMR method, only the height of the lower electrode needs to be controlled to move it near to the

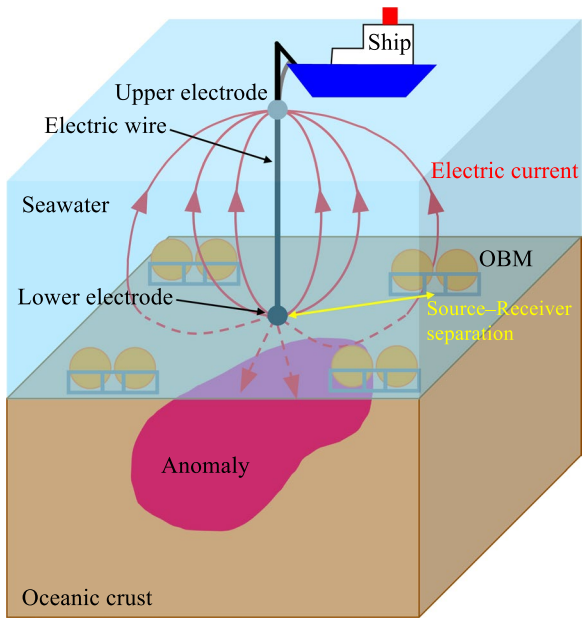

Fig. 1 A conceptual diagram of the magnetometric resistivity (MMR) method. An artificial vertical bipole source, composed of two electrodes and electric wires, conducts electric current from a lower electrode on the seafloor to an upper electrode at the sea surface in the case shown in this figure. OBMs, as receivers, measure the three components of the magnetic field variations induced by the bipole source on the seafloor

seafloor. As a result, surveys using the MMR method can be performed even for rough seafloor such as ridges.

In the simplest one-dimensional (1-D) model, the electrical resistivity of the oceanic crust is calculated from the relationship among the artificial electric current, the amplitude of the induced magnetic field, and the source–receiver separation. The full expression for the azimuthal magnetic field at the seafloor is given by Edwards et al. (1981). Assuming the contrast in resistivity between the seawater ρ_w and the oceanic crust ρ_c is large ($\rho_w \ll \rho_c$), and the source–receiver separation h is large compared to the water depth d ($h \gg d$), the approximate equation of the amplitude of the azimuthal component of the induced magnetic field B_θ is obtained in the cylindrical coordinate system with frequency set equal to zero:

$$B_\theta = \frac{\mu_o \rho_w d}{4\pi} \frac{I_{ext}}{h^2} \frac{1}{\rho_c} \tag{1}$$

where I_{ext} is the amplitude of the artificial electric current and μ_o is the magnetic permeability in vacuum (Edwards et al. 1981, 1984). This relation indicates that the amplitude of the induced horizontal magnetic field is inversely proportional to the square of the source–receiver separation. The amplitude of the induced magnetic field depends on the total electric current entering into the oceanic crust through an Ampère circuit centered on the source and passing through the receiver. Thus, the bulk electrical resistivity of the seafloor can be estimated from the amplitude of the induced magnetic field observed by the OBMs. Thus, if the oceanic crust were an insulator, the amplitude of the induced magnetic field would be zero because no electric current enters into the oceanic crust.

Surveys that use the MMR method have been conducted mainly for understanding the electrical resistivity structure of hydrothermal circulation systems on the spreading axes where the bathymetries are complex (e.g., Evans et al. 2002; Tada et al. 2005). These results, however, have only been analyzed assuming a 1-D resistivity structure using 1-D inversion code. That is, in the analysis it was assumed that the resistivity would change only toward the vertical direction and have constant electrical resistivity along the horizontal direction. Although 1-D inversion is a powerful method for speedy and rough analysis of structures beneath the seafloor, it is not sufficient to reveal the real electrical resistivity structures. This is because most of the targets, such as hydrothermal vents, representing conductive anomalies, and methane hydrates, representing resistive anomalies, have three-dimensional (3-D) shapes. These features contrast with the surrounding oceanic crust. Therefore, to reveal the 3-D resistivity structures beneath the seafloor as well as on land, we have developed a versatile 3-D forward code in the Cartesian coordinate system, applicable to both marine and terrestrial MMR methods.

For terrestrial resource exploration, numerical 3-D forward calculation methods have been proposed, primarily for MMR methods such as the surface MMR method (e.g., Chen et al. 2002) and the borehole MMR method (e.g., Abderrezak et al. 2017), because analytical solutions for the MMR method exist only in 1-D structures (Edwards et al 1981, 1984). These methods often discretize the equations using the finite volume method, defining the positions of electric currents at the cell faces. This approach sets the in/out currents of the subsurface at the cell faces as well as at the edges of the source wire. However, since the cross-sectional areas of the wires are generally much smaller than the cell size, the currents flowing through the wires are not defined at the cell faces but are separately calculated analytically to account for the magnetic fields they generate. Consequently, two different representations for the artificial currents entering and exiting are used: the cell face and the line.

We proposed utilizing nodes to accurately represent the currents entering the source wire at one location and exiting at another, as well as the currents moving in

and out of the subsurface. This approach allows all these currents to be precisely expressed at the corresponding nodes, enhancing the accuracy of our simulations. However, the locations where the source enters and exits become singular points in numerical calculations, posing significant challenges in computational analysis. The solution to this issue, which we developed while creating the 3-D forward code for the MMR method, is presented in Sect. 2. Although this paper primarily discusses applications to the marine MMR method, by altering the background resistivity structure, its adaptation for terrestrial MMR calculations also becomes feasible. In Sect. 3, we perform accuracy checks of the 3-D forward code. Section 4 presents tests conducted with typical synthetic examples for marine studies that feature an anomalous electrical resistivity body.

2 Development of 3-D forward modeling method

The essence of our 3-D forward calculation lies in extracting point-sources from the bipole source for computation, because the bipole source in the MMR method is represented by two point-sources of equal magnitude with opposite electrical signs accompanied by an electric current in a straight wire. When considering the 3-D electrical resistivity structure with designated point-sources, the relaxation method is employed to analyze the distribution of the electric potential. However, due to the singularities arising from the locations of the point-sources, accurate values cannot be computed for the current density when calculating it from the determined electric potential. To address this, two electrical resistivity structures are employed with point-sources placed at the same locations (e.g., Fig. 2b and c). The electric potential and current density are then determined for each structure separately. The discrepancy in current densities that arises from the variations in the structures is subsequently calculated, effectively offsetting the impact of the singularities. By deriving the magnetic field from this difference in current densities and combining it with the analytically calculated magnetic field generated by the bipole source for the simpler model (Fig. 2d in this case), the magnetic field for the 3-D electrical resistivity structure (Fig. 2a) observed by the OBM on the seafloor is determined. Further details are explained in the following paragraphs.

We discretize the entire computational domain in 3-D space and employ the finite volume method based on the control volume approach, which ensures the conservation of electric current, to calculate the electric potential (ϕ). In our approach, ϕ, B, and point-sources are chosen at the nodes of cubic cells. Each cell has constant electrical conductivity σ and the length of the cell edge is d, as shown in Fig. 3. Employing the control volume method implies that, except for the nodes where external currents (I_{ext}) may enter or exit as point-sources, the net electric current flow at all other nodes is zero. This equivalence ensures the conservation of current throughout the computational domain, except at the locations of point-sources. The conservation of electric current at a given node (i,j,k) can be written as:

$$I_x(i,j,k) + I_x(i+1,j,k) + I_y(i,j,k) + I_y(i,j+1,k) + I_z(i,j,k) + I_z(i,j,k+1) + I_{ext} = 0, \tag{2a}$$

$$I_{ext} = I_{ext}\delta(x - x_{out}, y - y_{out}, z - z_{out}) - I_{ext}\delta(x - x_{in}, y - y_{in}, z - z_{in}). \tag{2b}$$

Each electric current value can be expressed in terms of electric potentials and electrical conductivities as follows:

$$I_x(i,j,k) = \frac{1}{4}\{\sigma(i,j,k) + \sigma(i,j+1,k) + \sigma(i,j,k+1) + \sigma(i,j+1,k+1)\} \times \frac{\phi(i-1,j,k) - \phi(i,j,k)}{d} \times d^2, \tag{3a}$$

$$I_x(i+1,j,k) = \frac{1}{4}\{\sigma(i+1,j,k) + \sigma(i+1,j+1,k) + \sigma(i+1,j,k+1) + \sigma(i+1,j+1,k+1)\} \times \frac{\phi(i+1,j,k) - \phi(i,j,k)}{d} \times d^2, \tag{3b}$$

$$I_y(i,j,k) = \frac{1}{4}\{\sigma(i,j,k) + \sigma(i+1,j,k) + \sigma(i,j,k+1) + \sigma(i+1,j,k+1)\} \times \frac{\phi(i,j-1,k) - \phi(i,j,k)}{d} \times d^2, \tag{3c}$$

$$I_y(i,j+1,k) = \frac{1}{4}\{\sigma(i,j+1,k) + \sigma(i+1,j+1,k) + \sigma(i,j+1,k+1) + \sigma(i+1,j+1,k+1)\} \times \frac{\phi(i,j+1,k) - \phi(i,j,k)}{d} \times d^2, \tag{3d}$$

$$I_z(i,j,k) = \frac{1}{4}\{\sigma(i,j,k) + \sigma(i+1,j,k) + \sigma(i,j+1,k) + \sigma(i+1,j+1,k)\} \times \frac{\phi(i,j,k-1) - \phi(i,j,k)}{d} \times d^2, \tag{3e}$$

$$I_z(i,j,k+1) = \frac{1}{4}\{\sigma(i,j,k+1) + \sigma(i+1,j,k+1) + \sigma(i,j+1,k+1) + \sigma(i+1,j+1,k+1)\} \times \frac{\phi(i,j,k+1) - \phi(i,j,k)}{d} \times d^2. \tag{3f}$$

Here, we define six equations:

$$\sigma_x(i,j,k) = \frac{1}{4}\{\sigma(i,j,k) + \sigma(i,j+1,k) + \sigma(i,j,k+1) + \sigma(i,j+1,k+1)\}, \tag{4a}$$

$$\sigma_x(i+1,j,k) = \frac{1}{4}\{\sigma(i+1,j,k) + \sigma(i+1,j+1,k) + \sigma(i+1,j,k+1) + \sigma(i+1,j+1,k+1)\}, \tag{4b}$$

$$\sigma_y(i,j,k) = \frac{1}{4}\{\sigma(i,j,k) + \sigma(i+1,j,k) + \sigma(i,j,k+1) + \sigma(i+1,j,k+1)\}, \tag{4c}$$

$$\sigma_y(i,j+1,k) = \frac{1}{4}\{\sigma(i,j+1,k) + \sigma(i+1,j+1,k) + \sigma(i,j+1,k+1) + \sigma(i+1,j+1,k+1)\}, \tag{4d}$$

$$\sigma_z(i,j,k) = \frac{1}{4}\{\sigma(i,j,k) + \sigma(i+1,j,k) + \sigma(i,j+1,k) + \sigma(i+1,j+1,k)\}, \tag{4e}$$

$$\sigma_z(i,j,k+1) = \frac{1}{4}\{\sigma(i,j,k+1) + \sigma(i+1,j,k+1) + \sigma(i,j+1,k+1) + \sigma(i+1,j+1,k+1)\}. \tag{4f}$$

Solving this system using the relaxation method, with

In order to obtain $\phi(i,j,k)$, by substituting Eqs. (3a) through (3f) into Eq. (2a) and organizing the expressions,

$$\begin{aligned}\phi(i,j,k) = \{&(I_{ext}/d) + \sigma_x(i,j,k)\phi(i-1,j,k) + \sigma_x(i+1,j,k)\phi(i+1,j,k) + \sigma_y(i,j,k)\phi(i,j-1,k)\\ &+\sigma_y(i,j+1,k)\phi(i,j+1,k) + \sigma_z(i,j,k)\phi(i,j,k-1)\\ &+\sigma_z(i,j,k+1)\phi(i,j,k+1)\} \div \{\sigma_x(i,j,k) + \sigma_x(i+1,j,k)\\ &+\sigma_y(i,j,k) + \sigma_y(i,j+1,k) + \sigma_z(i,j,k) + \sigma_z(i,j,k+1)\}.\end{aligned} \tag{5}$$

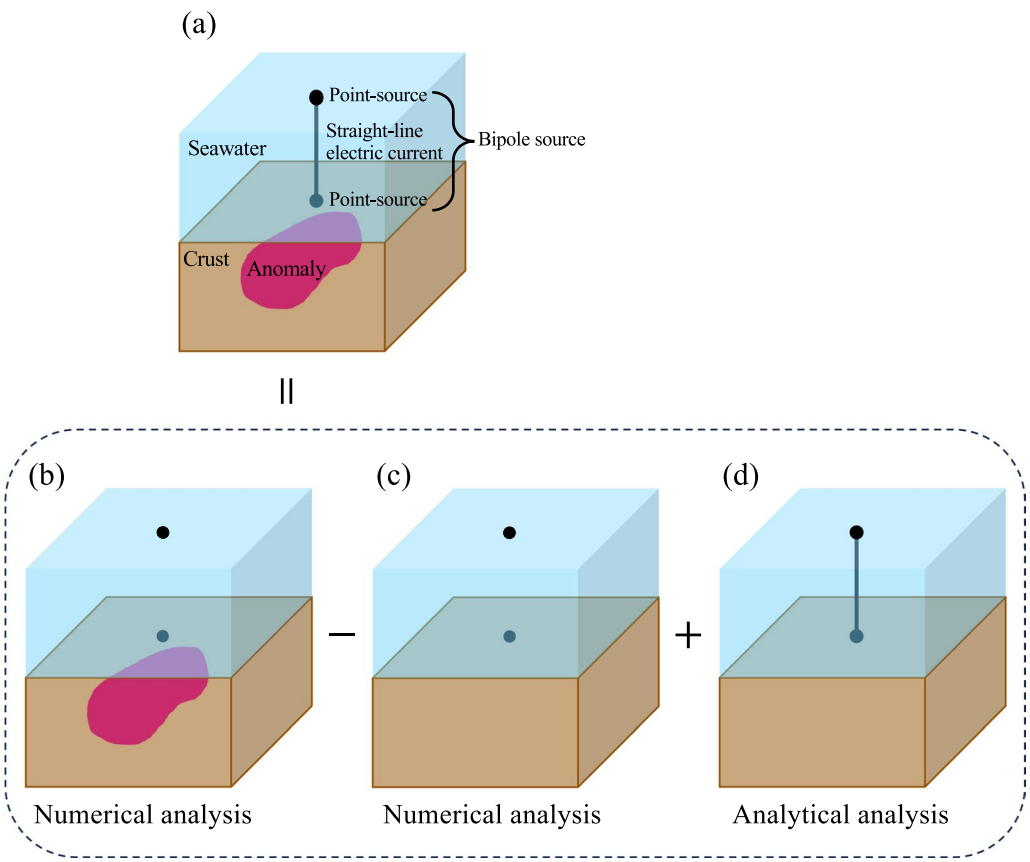

Fig. 2 Structures and sources used in the 3-D forward code. **a** A three-dimensional electrical resistivity structure, composed of seawater and oceanic crust layers, with an electrical resistive anomalous body embedded in the oceanic crust layer. A bipole source consists of a straight-line electric current and two point-sources: one at the sea surface and another on the seafloor. **b** The two point-sources are positioned as shown in **a**, within the three-dimensional electrical resistivity structure. **c** The two point-sources are positioned as shown in **a**, within a one-dimensional electrical resistivity structure composed of seawater and oceanic crust layer. **d** The bipole source is positioned as shown in **a**, within the one-dimensional electrical resistivity structure. In the figures, we have specified for each panel from **b** to **d** whether the calculations are performed using analytical or numerical solutions. In this study, current densities for panels **b** and **c** are calculated using the numerical analysis to determine the discrepancies. These discrepancies are then converted into magnetic field components by applying the Biot–Savart law. After obtaining stable magnetic field values, we add the magnetic field generated in panel **d**, as determined by the analytical solution, to calculate the observed magnetic field for panel **a**

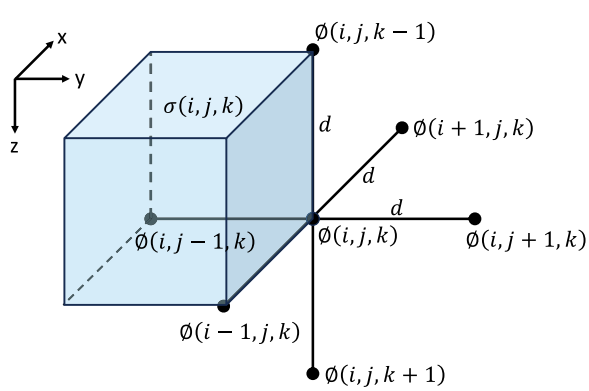

Fig. 3 A cell showing the locations for each variable. Each cell has a constant electrical conductivity $\sigma(i,j,k)$, where (i,j,k) denotes the position of the cell, and the length of each edge is d. Electric potentials are at the nodes

the boundary conditions described in the following paragraph, determines the distribution of the electric potential.

To ensure accurate and stable numerical results, we implemented two key conditions. First, we expanded the computational domain by adding a single layer of cells adjacent to each of the six outer faces and assigned specific resistivity values to these cells. This configuration effectively extends the computational domain far enough to enforce the boundary condition of $\phi = 0$ at every outer boundary, ensuring that the boundaries are sufficiently distant from the sources. We also set the electric potentials to zero at these outermost boundaries. Additionally, the electrical resistivities of the uppermost cells are set to infinity to represent air, an

insulating material. For the other five outermost sides, the electrical resistivities of the cells are modeled as semi-infinite seawater or oceanic crust to approximate the potential distribution found in analytical solutions. Accordingly, we assume the electrical conductivities within the cells on these five sides to be $\alpha \times \sigma_s$ and $\alpha \times \sigma_c$, respectively, adjacent to the seawater and the oceanic crust. Here, α is a real constant, and σ_s and σ_c are the electrical conductivities of the seawater and crust, respectively.

We used the simplest 1-D structure consisting of homogenous electrical conductivity to search for a suitable value of α because, as we mentioned earlier, there is only the 1-D analytical solution. The two point-sources are placed symmetrically with respect to a plane in the computational domain. Figure 4a shows a cross section of the electric potentials with the contours of the equipotential surface passing through the two point-sources of the computational domain for the analytical solution. When the boundary conditions correspond to a perfect conductor, i.e., in the case of $\alpha = \infty$, the contour of the potential surface closes within the computational domain (Fig. 4b). In contrast, when the boundary conditions correspond to an insulator, i.e., in the case of $\alpha = 0.00$, the contour shape of the potential surface undergoes deformation around the edges of the computational domain, deviating from the analytical solution (Fig. 4c). In particular, near the left and right boundaries, the analytical solution exhibits parabolic contour shapes, while the insulator exhibits inverse proportionality shapes. Taking into account the previously mentioned results and the fact that the contour plot of the potential at $\alpha = 1.00$ is nearly identical to that at $\alpha = \infty$, we investigated values of α in the range from 0 to 1. We found that there is no significant difference among 0.01, 0.07, and 0.5, but 0.07 is the most appropriate. Thus, we use $\alpha = 0.07$ for the second boundary conditions in this study (Fig. 4d).

The relaxation method is the simplest way to numerically solve a system of Poisson's equations for electric potential, which can include arbitrary electric point-sources under a given boundary condition. The relaxation method does not require large matrix operations; it merely iteratively updates the electric potential at each node to adjust the potentials of only the surrounding six nodes until no significant updates are observed across all the nodes. This approach significantly reduces both computational time and memory requirements, even for 3-D problems. However, there is a significant issue near the two point-sources because they manifest as singularities that give rise to substantial discrepancies between the analytical and numerical solutions in their proximity. The computational domain is discretized, and the discrepancies between them drop with the size of the cells. However, there is a trade-off between the size and number of the cell that directly affects the computational time, so we do not want to use a tiny cell. Furthermore, singular values occurring at the locations of the point-source cannot be eliminated, regardless of how small a cell is employed. Therefore, we conceived the idea of obtaining the electric potentials and the electric current densities of the two structures, and then taking the difference between the electric current densities, mitigating the disparity between numerical and analytical solutions. Taking the difference between the electric current densities obtained from the two structures and not between the electric potentials obtained from them is crucial to our method. This is because, when calculating the electric current density from the electric potential, the conductivity distributions of each structure are used, thus taking the difference in electric current densities allows us to bypass the use of conductivity distributions after the difference is taken.

Figure 5a and b illustrates two electrical resistivity structures used to verify the removal of the singular value influence caused by the point-sources by taking the difference in electric current density between the two structures. The computational domain is 5000×5000 m $\times 6000$ m^3, and the length of the cell used in both models is set to 50 m. The water depth of each model is constant at 3000 m, and the electrical resistivities of the seawater and oceanic crust are 0.3 and 6.0 Ω-m, respectively. Figure 5b has an anomaly layer with 2.0 Ω-m between the seawater layer and the crust. The first point-source was set above the sea surface, while the second one was positioned directly below the first one on the seafloor. We obtained the electrical current density distributions from the two structures using the aforementioned method.

Figure 5c and d depicts the current density vectors on the y–z cross-section for the structures represented in Fig. 5a and b, respectively. The y–z cross-section intersects the point-sources. The red arrows represent the computed results, with the arrow direction indicating that of the electrical current density vector and the length representing the magnitude of the electrical current density, normalized to the size of the black arrow. From these two figures, the following observations can be made. First, around the two point-sources, there exists a significantly large current density that spirals outward. In addition, the current density is higher in the seawater compared to within the crust. This is because the electrical resistivity of seawater is an order of magnitude smaller than that of the crust. In Fig. 5d, the influence of the anomaly layer on the electrical current density vectors should be present. However, the significant impact of singularities makes it challenging to discern differences based on the presence or absence of the anomaly layer by

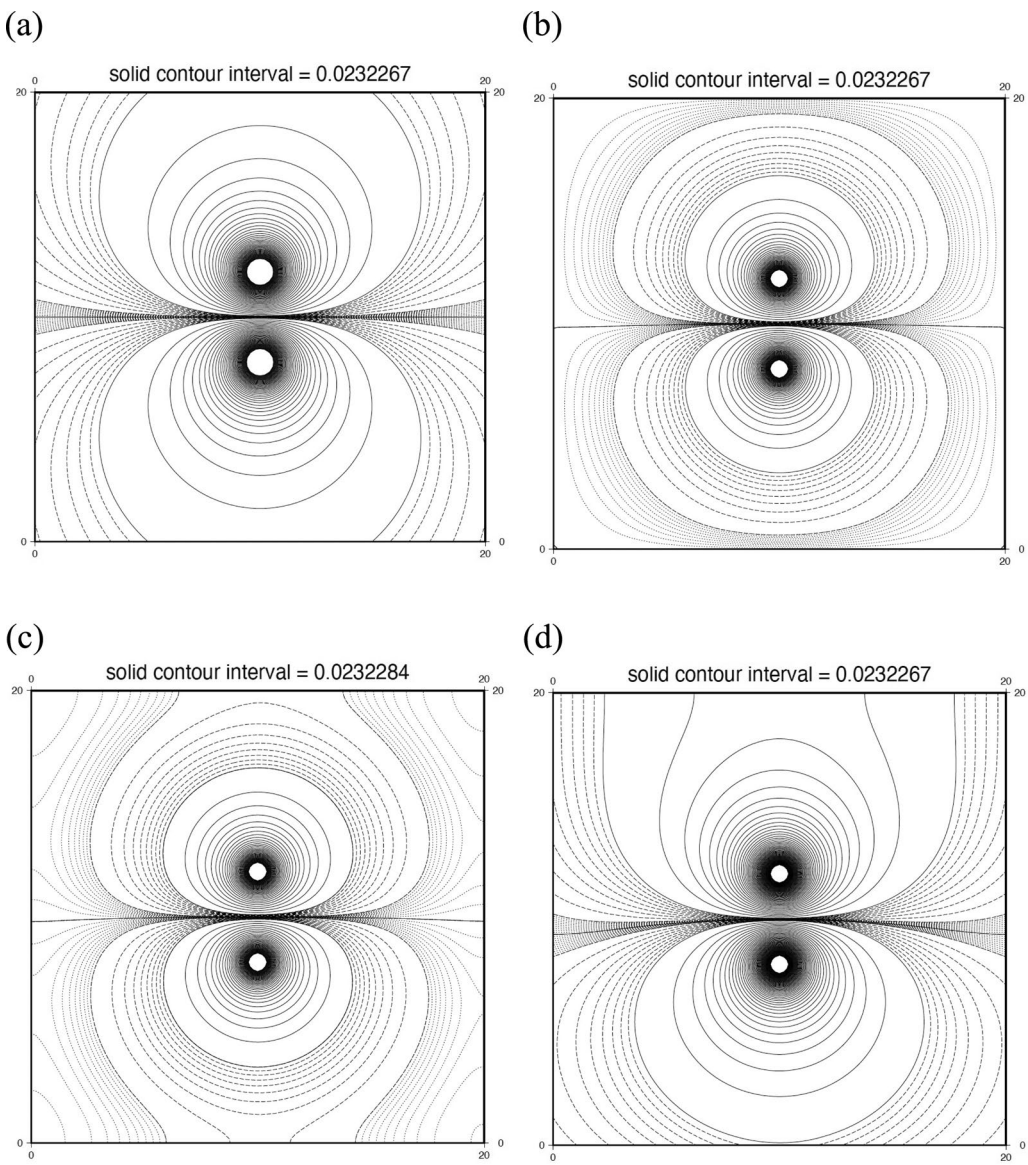

Fig. 4 Cross sections of the electric potentials passing through the two point-sources. **a** Analytical solution. **b** Numerical solution with the conductor boundary conditions. **c** Numerical solution with the insulator boundary conditions. **d** Numerical solution with boundary conditions using $\alpha = 0.07$

merely examining the plots in Fig. 5c and d. Thus, the y–z cross-section of the difference in electric current density obtained from the two structures (at the same location as Fig. 5c and d) is plotted in Fig. 5e. In Fig. 5e, large electric current density vectors remain near the point-source on the seafloor, while the extremely large electrical current density vectors near the point-source placed at the sea surface have disappeared. This indicates that the influence of singular values caused by the point-source at the sea surface has been neutralized. Therefore, it should be expected that the influence of singular values caused by the point-source on the seafloor has also been neutralized. The remaining large vector values near the seafloor are thus considered to represent the difference in electrical current density caused by the variations between the two structures.

The obtained difference in electric current density is transformed into magnetic field components by applying the Biot–Savart law, as expressed in the corresponding formula:

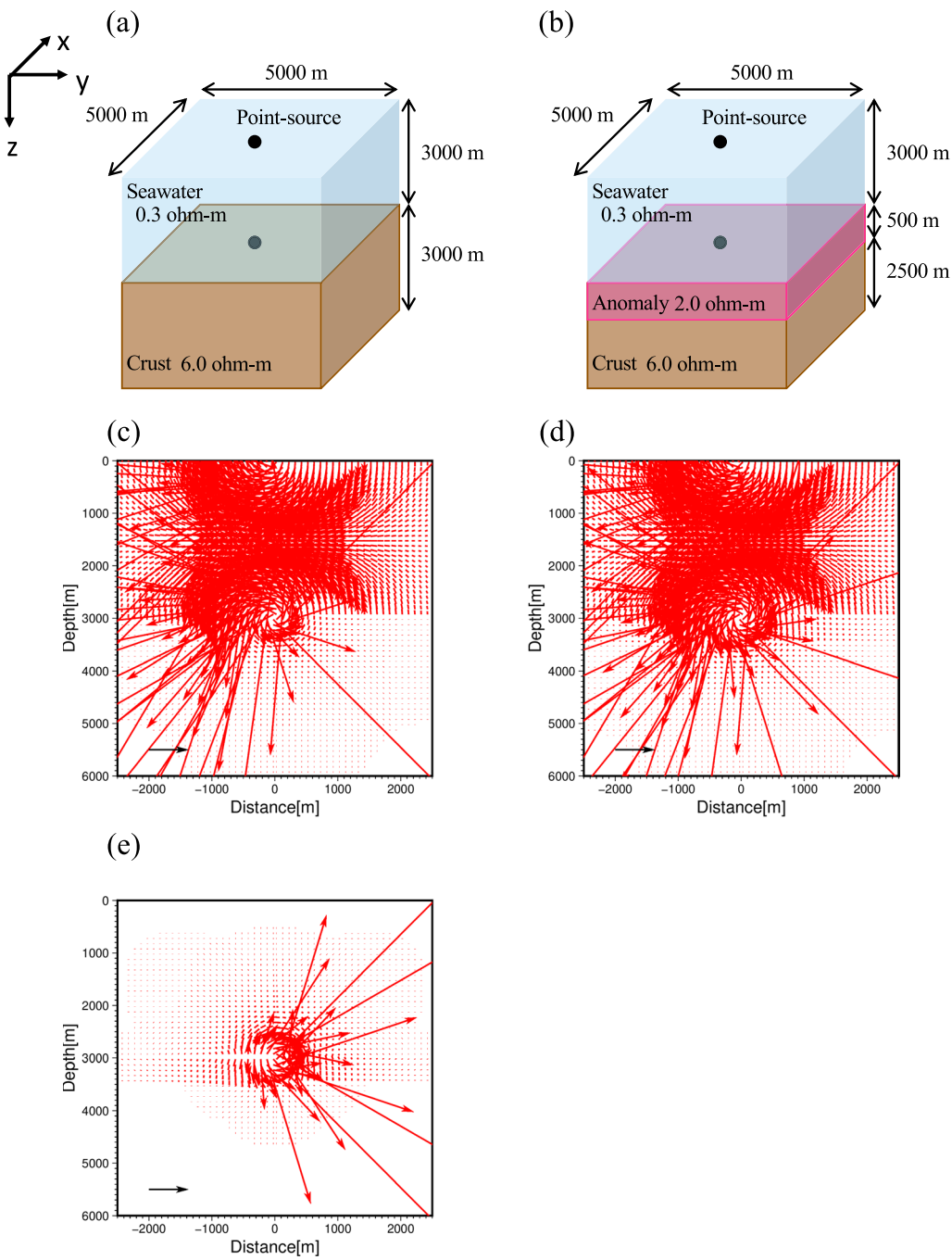

Fig. 5 Structures and computed results used to examine the impact of singular points. **a** Two-layer structure of seawater and oceanic crust. **b** Structure with an anomaly layer added to **a**. **c** Vector representation of the current density on the y–z cross-section obtained from the structure in **a**. **d** Vector representation of the current density on the y–z cross-section obtained from the structure in **b**. **e** Vector representation on the y–z cross-section of the difference between the current densities from **d** and **c**. **c** to **e** Depict the y–z cross-section at $x = 2500$m. The size of each vector is normalized to the magnitude of the black arrow

$$d\boldsymbol{B}(\boldsymbol{r}) = \frac{\mu_0}{4\pi} \oint d^3\boldsymbol{r}' \frac{d\boldsymbol{J}(\boldsymbol{r}') \times (\boldsymbol{r} - \boldsymbol{r}')}{|\boldsymbol{r} - \boldsymbol{r}'|^3}, \tag{6}$$

where $\mathrm{d}\boldsymbol{J}(\boldsymbol{r})$ represents the three components of the difference in electric current density at $\boldsymbol{r}$, with $\boldsymbol{r}$ being defined as the center of each cell. The resulting magnetic field, $\mathrm{d}\boldsymbol{B}(\boldsymbol{r})$, represents only the magnetic field

difference induced by placing point-sources in the two types of electrical resistivity structures (Fig. 2b, c). Hence, to determine the magnetic field variations observed when a bipole source is applied in a 3-D electrical resistivity structure, it is necessary to add the magnetic field induced by a bipole source through the simpler of the two structures. Choosing a 1-D electrical resistivity structure as in Fig. 2d as the simpler counterpart allows for the calculation of the magnetic field induced by applying a bipole source to that structure using analytical solutions. One-dimensional analytic forward codes for a vertical bipole source have already been developed (e.g., Edwards et al. 1984; Evans et al. 2002). We use the code by Evans et al. (2002) to calculate the magnetic field, $\boldsymbol{B}^{1D}(\boldsymbol{r})$, induced by a vertical bipole source. Finally, the magnetic field $\boldsymbol{B}^{3D}(\boldsymbol{r})$ observed by the OBM on the seafloor when a bipole source is applied to the 3-D structure can be determined by:

$$\boldsymbol{B}^{3D}(\boldsymbol{r}) = \boldsymbol{B}^{1D}(\boldsymbol{r}) + d\boldsymbol{B}(\boldsymbol{r}) \tag{7}$$

3 Accuracy checks of the 3-D forward modeling method

For the validation of the accuracy of the developed 3-D forward code, we compared the results with those obtained from the 1-D forward code (Evans et al. 2002). In this comparison, the two models illustrated in Fig. 6a, b were utilized. The length of the cell used in both models was set to 50 m. Figure 6a is a layered structure that includes an anomaly layer on the oceanic crust. The model represented in Fig. 6b features a half-space structure beneath the seafloor, or in other words, it lacks the anomaly layer present in the model depicted in Fig. 6a. Hereafter, we refer to the model in Fig. 6b as the background model. The water depth of each model is a constant 3000 m, and the electrical resistivities of the seawater and the oceanic crust are 0.3 and 6.0 Ω-m, respectively. The electrical resistivity of the anomaly layer depicted in Fig. 6a is set to either 2.0 Ω-m or 20 Ω-m, with a thickness of 500 m. Two point-sources are located as a vertical bipole source at the center of the computational region; one source is located at the sea surface (the upper point-source) and the other is on the seafloor (the lower point-source). Receivers are set on all nodes at the same level of the seafloor except the location of the lower point-source, so receivers are located every 50 m from the lower point-source to the edge of the computational domain. Three different dimensions of the computational domain are employed. The vertical length is fixed at 6000 m, while the horizontal lengths are 4000, 5000, or 6000 m.

In our synthetic tests, we primarily used resistivity values derived from prior studies involving MMR methods. Tada et al. (2005) reported oceanic crust resistivities near the seafloor of approximately 6.0 Ω-m, a value we adopted as the background resistivity for this study. This value is particularly relevant as it corresponds to the spreading axis environment targeted in our research, providing a realistic basis for our synthetic tests. This aligns with findings from other studies: Nobes et al. (1986) reported a basalt half-space resistivity of 8.5 Ω-m, Evans et al. (1998) recorded 10 Ω-m, and Evans et al (2002) observed approximately 6.0 Ω-m beneath the on-axis area. More recent CSEM studies have shown resistivity at the surface around 10 Ω-m, increasing to approximately 60 Ω-m at 1 km depth, with values ranging from 60 to 1000 Ω-m or more at deeper levels (Naif et al. 2015). This pattern is corroborated by downhole logging measurements, which also indicate increasing resistivities with depth. Specifically, resistivities at DSDP Hole 504B reach up to 500 Ω-m at about 1000 m below seafloor (mbsf) (Becker 1985), and at IODP Hole U1439C, they increase from 4 Ω-m at about 180 mbsf to about 100 Ω-m at about 330 mbsf (Reagan et al. 2015). Thus, while our study assumes a uniform background resistivity of 6.0 Ω-m at the basement top to simplify the synthetic model, it is clear that resistivities typically increase with depth. Investigating the behavior of model responses using a more realistic, depth-varying, layered structure for background resistivity remains an important area for future research.

The electrical resistivity of the anomaly layer is set to equal ratios to the background value of 6.0 Ω-m so that one can easily expect the results in the cases of further anomalous values by simple visual extrapolation. In this context, we use electrical resistivity values of 2.0 Ω-m and 20 Ω-m for the anomalous body. These values are, respectively, half an order of magnitude (approximately $\sqrt{10}$ times) more conductive or resistive than the background, when considered on a logarithmic scale. The electrical resistivity of 2.0 Ω-m for the conductive anomaly roughly corresponds to the sedimentary layer with an electrical resistivity of 1.9 Ω-m and a thickness of 560 m, as reported by Edwards et al. (1985). The thickness of our anomaly layer, depicted in Fig. 6a, is also based on the findings of Edwards et al. (1985). Meanwhile, the electrical resistivity value of 20 Ω-m for the resistive anomaly corresponds closely to the electrical resistivity of approximately 20 Ω-m observed more than 200 m beneath the off-axis area, as reported by Evans et al. (2002). The resistivity value of seawater is generally set to 0.3 Ω-m, which is consistent with the results reported by Tyler et al. (2017).

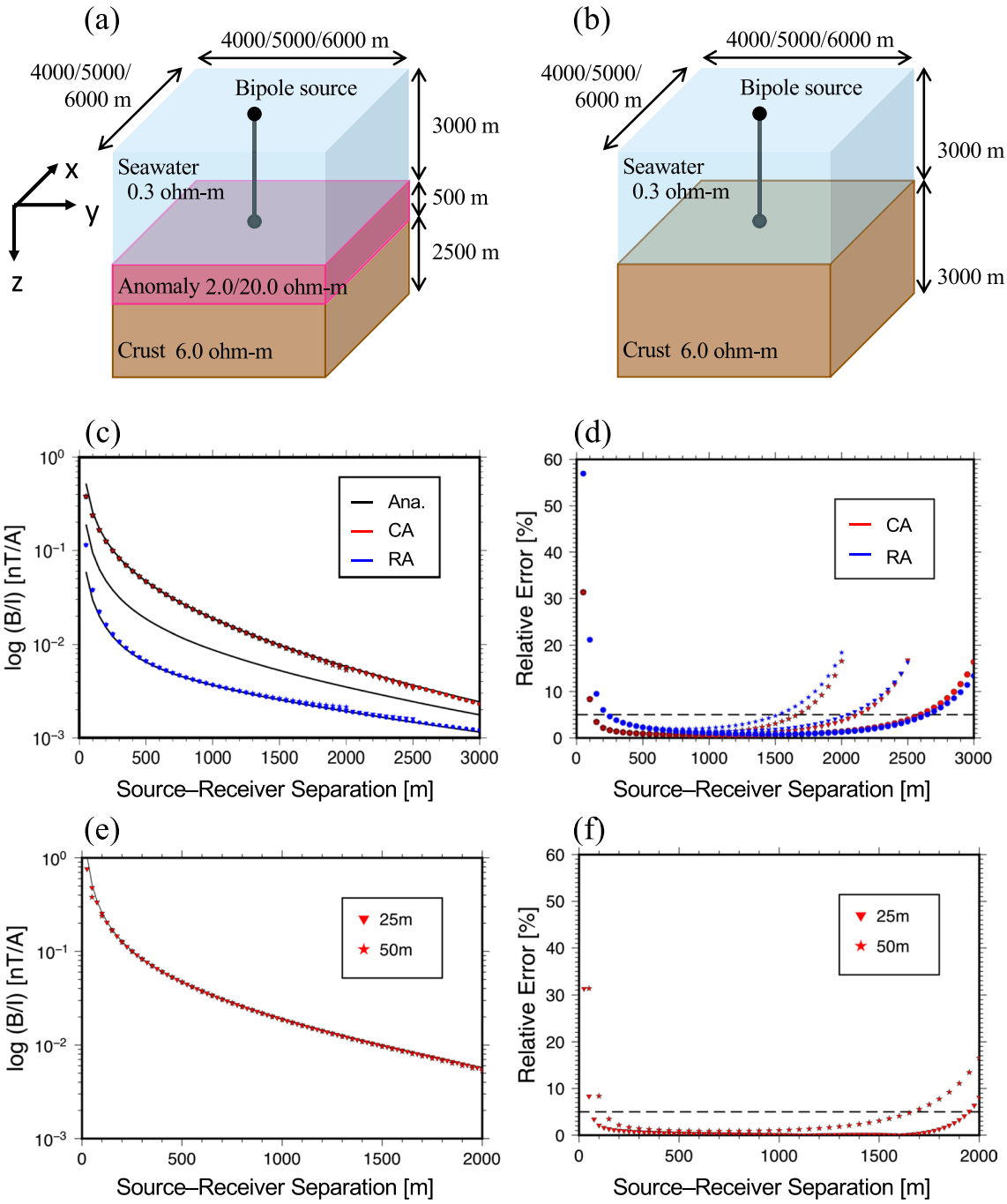

Fig. 6 Structures and results used for the accuracy verification of the 3-D forward code. **a** Three-layered structure: seawater, anomaly layer, and the oceanic crust. The water depth is 3000 m, and the thickness of the anomaly layer is 500 m. The location of the bipole source is at the center in the horizontal plane. **b** The two-layered structure used as the background model. **c** Logarithm of the total magnetic field normalized by the electric current value. Black lines are results by using the 1-D forward code, and colored symbols are by using the 3-D forward code. Red symbols are the results for the 3-D models with the conductive anomaly (CA), and blue symbols are those for the 3-D models with the resistive anomaly (RA). The symbol shapes indicate the sizes of the computational domain: $4000 \times 4000 \times 6000$ m^3 (stars), $5000 \times 5000 \times 6000$ m^3 (inverted triangles), and $6000 \times 6000 \times 6000$ m^3 (circles). The cell size is 50 m, and OBMs are located at every vertex of the control volume on the seafloor. **d** The relative errors calculated using Eq. (7) in the case of **c**. The colors and shapes of the symbols are the same as in **c**. **e** Logarithm of the total magnetic field normalized by the electric current value. The black line is the result of the 1-D forward code, and red symbols are the results of the 3-D forward code for the 3-D model with the conductive anomaly. The size of the computational domain is $4000 \times 4000 \times 6000$ m^3. Stars indicate the simulation results obtained using 50-m cells, and inverted triangles indicate those obtained using 25-m cells. **f** The relative errors in the case of **e**. The symbols indicate the same as in **e**

Figure 6c shows the amplitude of the magnetic field observed in the models with respect to the distance between the lower point-source and receiver (hereafter, Source–Receiver (S–R) separation). The black lines indicate the analytical solutions by Evans et al. (2002) for the model with the conductive anomaly layer (upper line), the background model (middle line), and the model with the resistive anomaly layer (lower line). The red and blue symbols represent values obtained using the 3-D forward code developed in this study. The red symbols correspond to calculations for the model with the conductive anomaly layer, while the blue symbols correspond to calculations for the model with the resistive anomaly layer. The shapes of the symbols vary based on the horizontal length of the computational domain, with stars representing a horizontal length of 4000 m, inverted triangles representing 5000 m, and circles representing 6000 m. From this figure, the results from the 3-D forward code exhibit consistent agreement with the analytical solutions except for the S–R separation of 50 m and edges of the computational domain, regardless of the horizontal size of the computational domain or the electrical resistivity value of the anomaly layer.

To further investigate the slight discrepancies observed in Fig. 6c, specifically in the vicinity of the bipole source and towards the boundaries of the computational domain, the relative error with the analytical solution as the denominator was calculated using the following formula:

$$\varepsilon(\boldsymbol{r}) = \left| \frac{\boldsymbol{B}^{num}(\boldsymbol{r}) - \boldsymbol{B}^{ana}(\boldsymbol{r})}{\boldsymbol{B}^{ana}(\boldsymbol{r})} \right| \times 100, \tag{8}$$

where $\varepsilon(\boldsymbol{r})$, $\boldsymbol{B}^{num}(\boldsymbol{r})$, and $\boldsymbol{B}^{ana}(\boldsymbol{r})$ represent the relative error, numerical solution, and analytical solution of the magnetic field induced by the bipole source, respectively.

Relative errors with respect to the S–R distance are plotted in Fig. 6d, in which the same colors and symbols as in Fig. 6c indicate the electrical resistivity values of the anomaly layer and the size of the computational domain. This plot of relative errors allowed us to examine the trends in the discrepancies between the analytical solution and the numerical results near the bipole source and towards the boundaries of the computational domain. The relative errors around the bipole source and close to the edges are larger than 10%, regardless of the size of the computational domain. In particular, regardless of the size of the computational domain, when the S–R separation is less than 150 m, the relative error becomes significantly large. However, the magnitude of this error, which increases as the distance decreases, remains constant, independent of the size of the computational domain, when the S–R separation is the same, or if the number of cells from the point-source is the same. From these findings, the significant error near the bipole source is attributed not to the boundary conditions of the 3-D forward code developed in this study, but rather to the influence of the point-source. However, the substantial relative error near the boundaries of the computational domain can be explained by the impact of the boundary conditions. For instance, assuming the threshold for relative error is set at 5%, irrespective of the computational domain size, the relative error exceeds the threshold up to a distance 500 m from the boundaries, which is within the range of the first 10 cells from the boundaries. Therefore, when using this 3-D forward code in practical applications, it is advisable to set the computational domain size to be at least 500 m larger than the intended area of interest, or to add at least 10 cells outside the intended area of interest.

We investigated whether the high relative errors near the bipole source were due to the distance from the point-source or the number of cells from the point-source. To examine this, we compared the results for a model with the conductive anomaly layer in a computational domain size of $4000 \times 4000 \times 6000$ m^3. We considered two cell sizes: 50 m and half of that, 25 m. The magnetic field values from the computational results are depicted in Fig. 6e, and the relative error values in Fig. 6f. The star symbol represents the results obtained using the 50-m cell, while the inverted triangle symbol represents the results obtained using the 25-m cell. According to Fig. 6e, the results using different cell sizes are highly consistent, except for cases where the S–R separation is less than 100 m. When examining the differences in relative errors in more detail, it is observed that the relative errors near the first and second closest locations to the bipole source are nearly the same, regardless of the cell size, and both exceed 5%. Based on the above, it is evident that the high relative error near the bipole source is not due to the distance from the bipole source, but rather due to the number of cells. Therefore, when using the 3-D forward code in practice, results within a distance of two cells from the bipole source should not be considered.

From the comparison of relative errors in Fig. 7f, it is evident that using smaller cells results in lower relative errors in areas away from the bipole source. This suggests an improvement in computational accuracy when smaller cells are employed. The enhancement in accuracy is particularly noticeable near the boundaries of the computational domain. The relative error exceeds 5% within the initial 300 m from the boundary when using a 50-m cell, while with a 25-m cell, this exceeds 5% solely within the initial 50 m from the boundary, indicating a significant

improvement. Expressed in terms of the number of cells, exceeding 5% near the boundaries occurs within the initial 7 cells when using a 50-m cell and within the initial 2 cells when using a 25-m cell. This implies that the impact of boundary conditions on numerical computations can be improved by reducing the size of cells. However, there is a trade-off, as reducing the cell size increases the number of cells and, consequently, the computation time. The decision on how small to make the cells should be based on a trade-off between the required computational domain and the associated computation time.

4 Synthetic tests using the 3-D forward modeling method

In the MMR method, OBMs are deployed on the seafloor to measure the magnetic field generated by applying a vertical bipole source to explore the electrical resistivity structure beneath the seafloor. The observed data are then analyzed to investigate the resistivity distribution beneath the seafloor. This study enables 3-D forward modeling for the MMR method, making it possible to predict the magnetic field observed by the OBMs when the structure beneath the seafloor is three-dimensional. The 3-D forward code we developed is characterized by the performance of calculations using two models: a background model representing a 1-D electrical resistivity structure and a 3-D electrical resistivity structure model incorporating anomalies. To investigate the variations in the magnetic field observed by the OBMs when a bipole source is applied to the background model and the 3-D model with anomalies, we define the magnetic field anomaly $\Delta\boldsymbol{B}$ as follows:

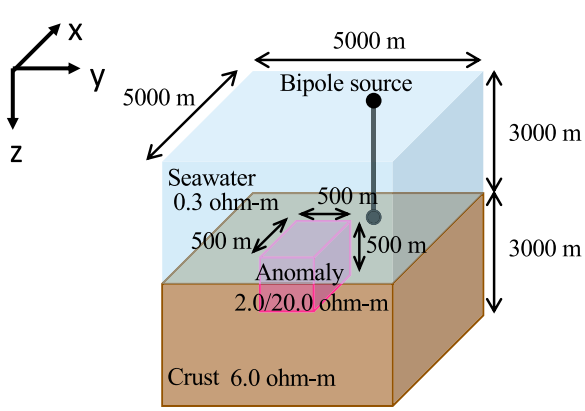

Fig. 7 The 3-D electrical resistivity structure used in the synthetic test for the 3-D forward code. The computational domain is $5000\times5000\times6000$ m^3, with a water depth is 3000 m, and is discretized using 50-m cells. The conductive anomaly or resistive anomaly is buried in the oceanic crust, with the top of the anomalous body at the same level as the seafloor. The size of the anomalous body is $500\times500\times500$ m^3

$$\Delta\boldsymbol{B}(\boldsymbol{r}) = \log\boldsymbol{B}^{3D}(\boldsymbol{r}) - \log\boldsymbol{B}^{1D}(\boldsymbol{r}) = \log\frac{\boldsymbol{B}^{3D}(\boldsymbol{r})}{\boldsymbol{B}^{1D}(\boldsymbol{r})} = \log\frac{\boldsymbol{B}^{1D}(\boldsymbol{r}) + d\boldsymbol{B}(\boldsymbol{r})}{\boldsymbol{B}^{1D}(\boldsymbol{r})}. \tag{9}$$

As depicted in Fig. 6c, the amplitude of the magnetic field generated by the bipole source varies on a logarithmic scale with S–R separation. Therefore, from this point onward, the magnetic field anomaly is treated on a logarithmic scale.

The amplitude and the distribution of the magnetic field anomaly should be related to the electrical resistivity values, sizes, and shapes of the anomalous electrical resistivity body, hereafter referred to as the anomalous body, and/or the relative position of the bipole source to the anomalous body. To elucidate the relationship between the magnetic field anomaly and the anomalous body, we conducted synthetic tests using simple 3-D models. In these models, a cubic anomalous body with electrical resistivity higher or lower than that of the oceanic crust is positioned at the center of the computational domain. The anomalous body is situated within the oceanic crust, and its upper surface coincides with the seafloor (Fig. 7). The background model for the synthetic tests is the same as in Fig. 6b, consisting of a two-layer structure representing seawater and oceanic crust. All models used for the synthetic tests have a computational domain size of $5000\times5000\times6000$ m^3, with a cell size of 50 m. Consequently, the number of cells is $100\times100\times120$. The water depth is kept constant at 3000 m, so the top 60 cells in the vertical direction represent seawater, and the remaining cells represent either oceanic crust or the anomalous body. The resistivity values for seawater and oceanic crust are 0.3 and 6.0 Ω-m, respectively. The size of the anomalous body is $500\times500\times500$ m^3, equivalent to $10\times10\times10$ cells. The resistivity of the anomalous body is set to either 2.0 Ω-m or 20 Ω-m. From here on, we refer to the 3-D model containing the anomalous body with a resistivity of 2.0 Ω-m as the conductive anomaly (CA) model, and the model with the anomalous body having a resistivity of 20 Ω-m as the resistive anomaly (RA) model. The current flowing through the bipole source is normalized to 1 A for standardization.

In the synthetic tests, two types of calculations were performed. The first involved a single bipole source, while multiple OBMs simultaneously observed the magnetic field. This case, referred to as Type I, entails plotting the calculated magnetic field anomaly values at the positions of the respective OBMs that observed the anomaly. Magnetic field anomalies were calculated for the positions of the bipole source at $(0,0)$, $(100,0)$, $(250,0)$, $(500,0)$, $(1000,0)$, and $(1500,0)$

with the center of the computational domain set at (0, 0). A total of 6560 locations were used to calculate the magnetic field anomaly for each case, and the results are shown in Figs. 8 and 9. The second type involved placing an OBM in a single location and observing the magnetic field when the bipole source was applied from various locations. This configuration, termed Type II, involves plotting the calculated magnetic field anomaly values at the positions where the OBM observed the anomaly when the bipole source was active. Magnetic field anomalies were calculated for the positions of the OBM at (0, 0), (100, 0), (250, 0), (500, 0), (1000, 0), and (1500, 0). A total of 1598 locations were used for each case in which the bipole source was energized. The results are depicted in Figs. 10 and 11.

Figures 8 through 11 depict horizontal cross-sections plotting the values of the magnetic field anomaly calculated through the synthetic tests. Contour intervals are set at 0.01. Locations where the magnetic field anomaly is positive and exceeds 0.1 are highlighted in red, while those with negative anomaly values below –0.1 are shaded in blue. The stars on the plane indicate the positions of the bipole source, and the open circles represent the locations of the OBM. Figure 8 displays the Type I results for the CA model, Fig. 9 illustrates the Type I results for the RA model, Fig. 10 depicts the Type II results for the CA model, and Fig. 11 presents the Type II results for the RA model.

The most significant feature is that the magnetic field anomaly for the CA model is positive in the cases of both Type I and Type II. Similarly, the magnetic field anomaly for the RA model is negative in both scenarios. Therefore, by determining the sign of the magnetic field anomaly, it is possible to infer whether the electrical resistivity of the anomalous body beneath the seafloor is higher or lower.

From this point onward, we analyze the regions where the absolute value of the magnetic field anomaly exceeds $\left|\log(\Delta B/I)\right| \geq 0.1$, 1.25 nT/A for the CA model and 0.79 nT/A for the RA model, respectively (i.e., the colored regions in Figs. 8, 9, 10 and 11). This focus is justified because the noise level of the OBMs during the MMR experiments ranged from approximately 0.003 to 0.02 nT/A (Tada et al. 2005; Matsuno et al. 2015), making it feasible to detect these anomalies using OBMs. When the OBM or bipole source is positioned above the anomalous body, as in cases (a) to (c) in each figure, the area with an absolute value greater than 0.1 extends beyond the anomalous body's outer boundary. In this context, Type I tends to have a broader extent than Type II. Additionally, there is a tendency for the CA model to exhibit a wider area than the RA model. When the OBM or bipole source is located outside the anomalous body, as in cases (d) to (f) in each figure, the area with an absolute value greater than 0.1 becomes either equal to or smaller than the size of the anomalous body. Comparing within each Type, the CA model tends to have a wider region than the RA model, because electric current flows into the oceanic crust more easily in the CA model than in the RA model, which increases the magnetic field. These comparisons indicate that in the MMR method, there is a greater sensitivity to lower resistive anomalous bodies than higher resistive anomalous bodies.

When the OBM or bipole source is located outside the anomalous body, that is, in cases (d) to (f) in each figure, comparing the areas with an absolute value greater than 0.1 between Type I and Type II of the same model shows that Type II tends to have a wider region than Type I. These results indicate that when either the transmitting bipole source or the receiving OBM is the only one present on the anomalous body, having the bipole source above the anomalous body results in a larger magnetic field anomaly, suggesting better exploration efficiency. This is a significant advantage when conducting exploration with the MMR method because increasing the number of bipole source locations is much easier than increasing the number of OBMs. The method of increasing bipole source locations is discussed in a study by Seama et al. (2013), which demonstrated the advantages of a continuously towed bipole source compared to the conventional vertical bipole source that we employ in this paper. The towed bipole source, despite being inclined at approximately 8 degrees from the vertical during towing, exhibited a magnetic field magnitude comparable to that of the vertical bipole source. This suggests that the towed bipole source allows for an easier increase in source positions while maintaining a magnetic field strength comparable to the conventional setup.

Our developed 3-D forward modeling method was applied to the observed MMR responses obtained near a hydrothermal vent called the Snail site on the ridge crest of the Southern Mariana Trough (Matsuno et al. 2015). Using Eq. (9) and a background model estimated by Edwards et al. (1981), Matsuno et al. (2015) calculated the distribution of magnetic field anomalies and obtained the optimal 3-D electrical resistivity structure by iteratively refining the method. Matsuno et al. (2015) identified six anomalous bodies beneath the seafloor, one of which is a conductive anomaly directly beneath the Snail site, interpreted as hydrothermal fluid. The adjacent resistive anomalies were explained as areas of low porosity. To further substantiate these results and enhance broader applicability, developing an inversion process that can efficiently determine the 3-D electrical resistivity structure beneath the seafloor is a critical part of our future work. This process will integrate our developed 3-D forward code and is intended for general use in diverse geological settings.

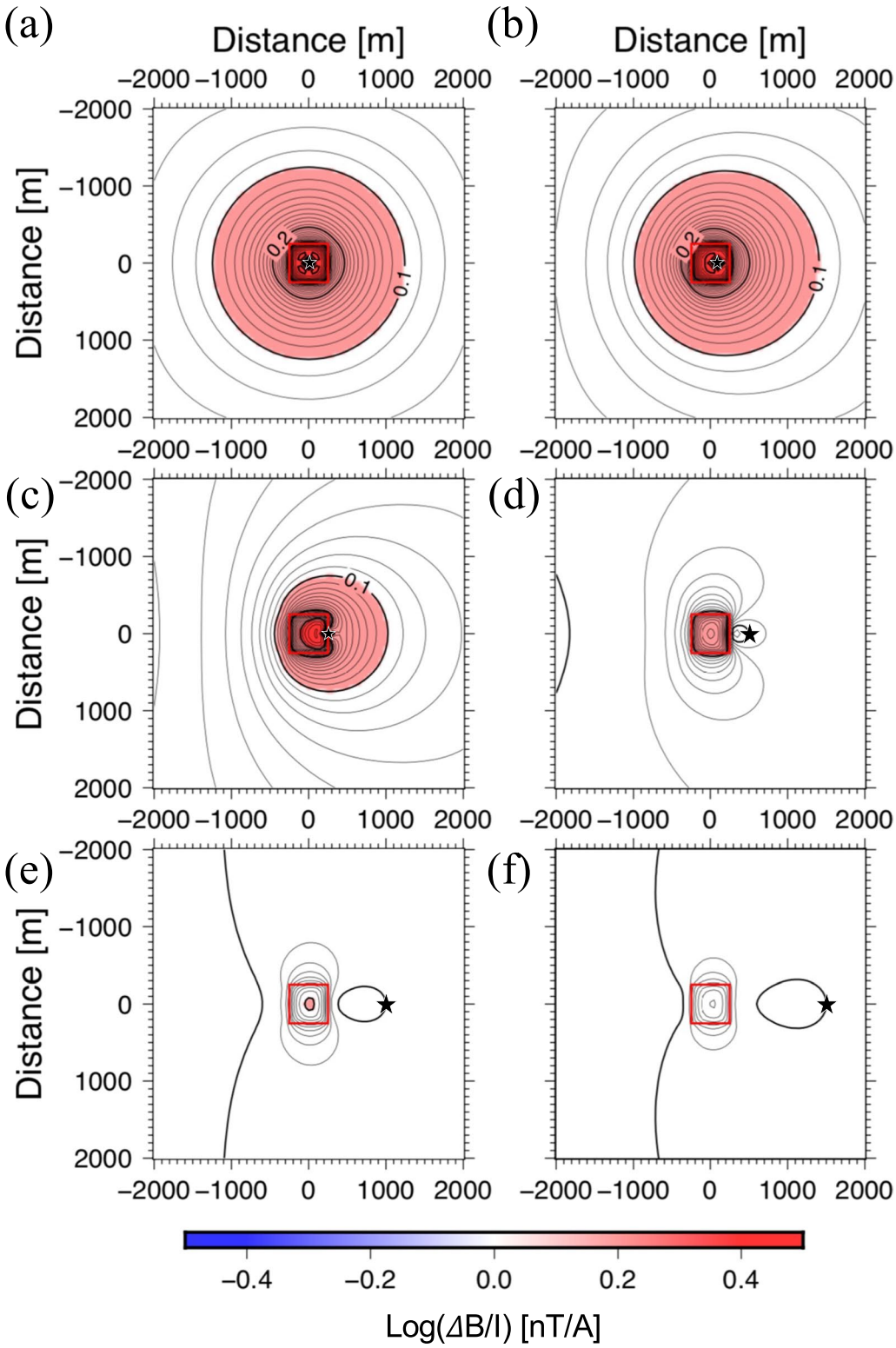

Fig. 8 Type I magnetic field anomaly for the CA model. The red squares and black stars indicate the positions of the conductive anomalous bodies and the bipole sources, respectively. Contours are plotted every log0.01 [*n*T/A]. Color indicates the sign and amplitude of the magnetic field anomaly. **a** Bipole source on the center of the anomalous body, (0, 0). **b** Bipole source on the anomalous body at (100, 0). **c** Bipole source on the edge of the anomalous body, (250, 0). **d** Bipole source not on the anomalous body, (500, 0). **e** Bipole source located at (1000, 0). (f) Bipole source located at (1500, 0)

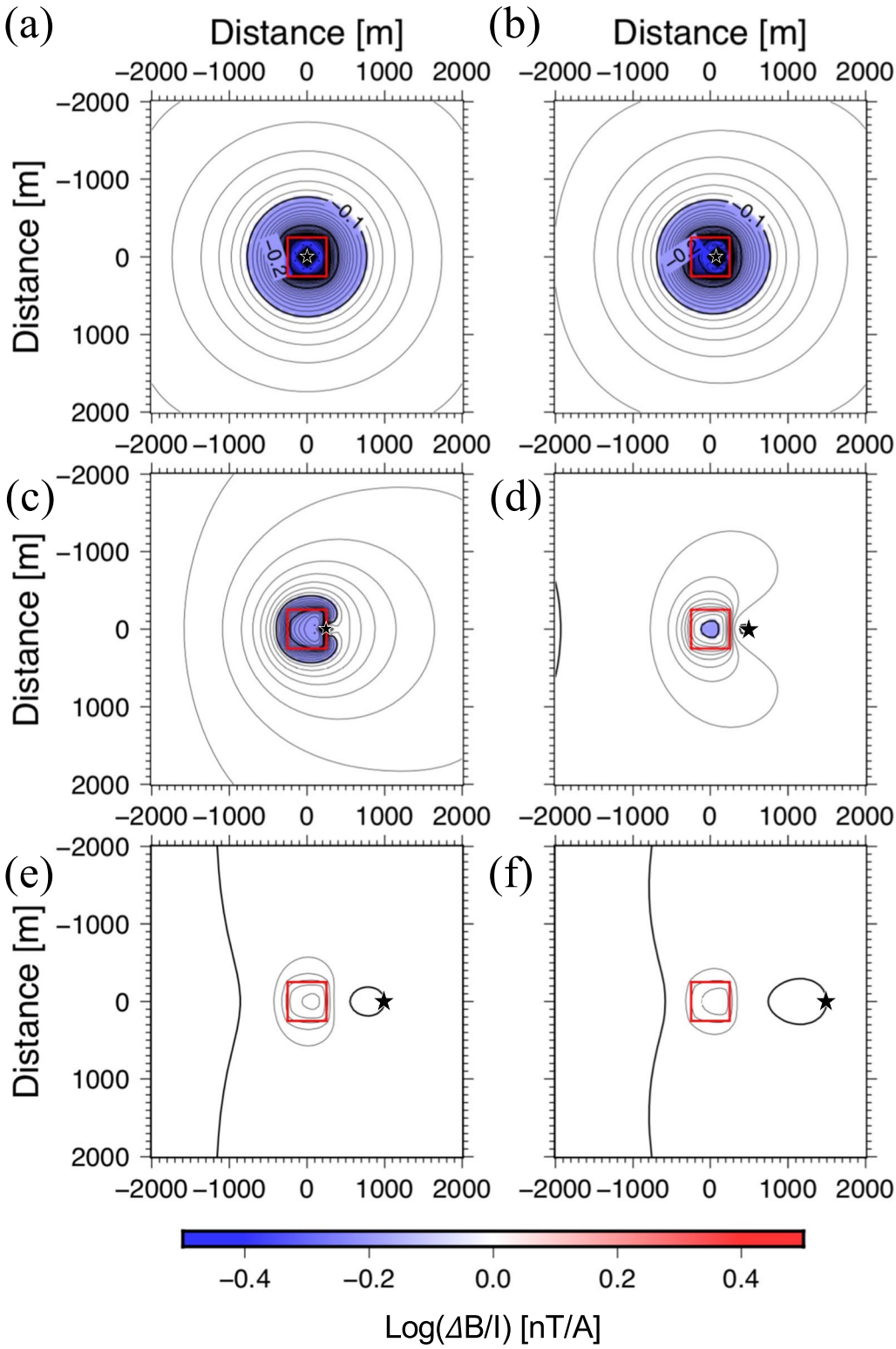

Fig. 9 Type I magnetic field anomaly for the RA model. **a-f** All conditions except for the electrical resistivity value of the anomalous body are the same as those in Fig. 8

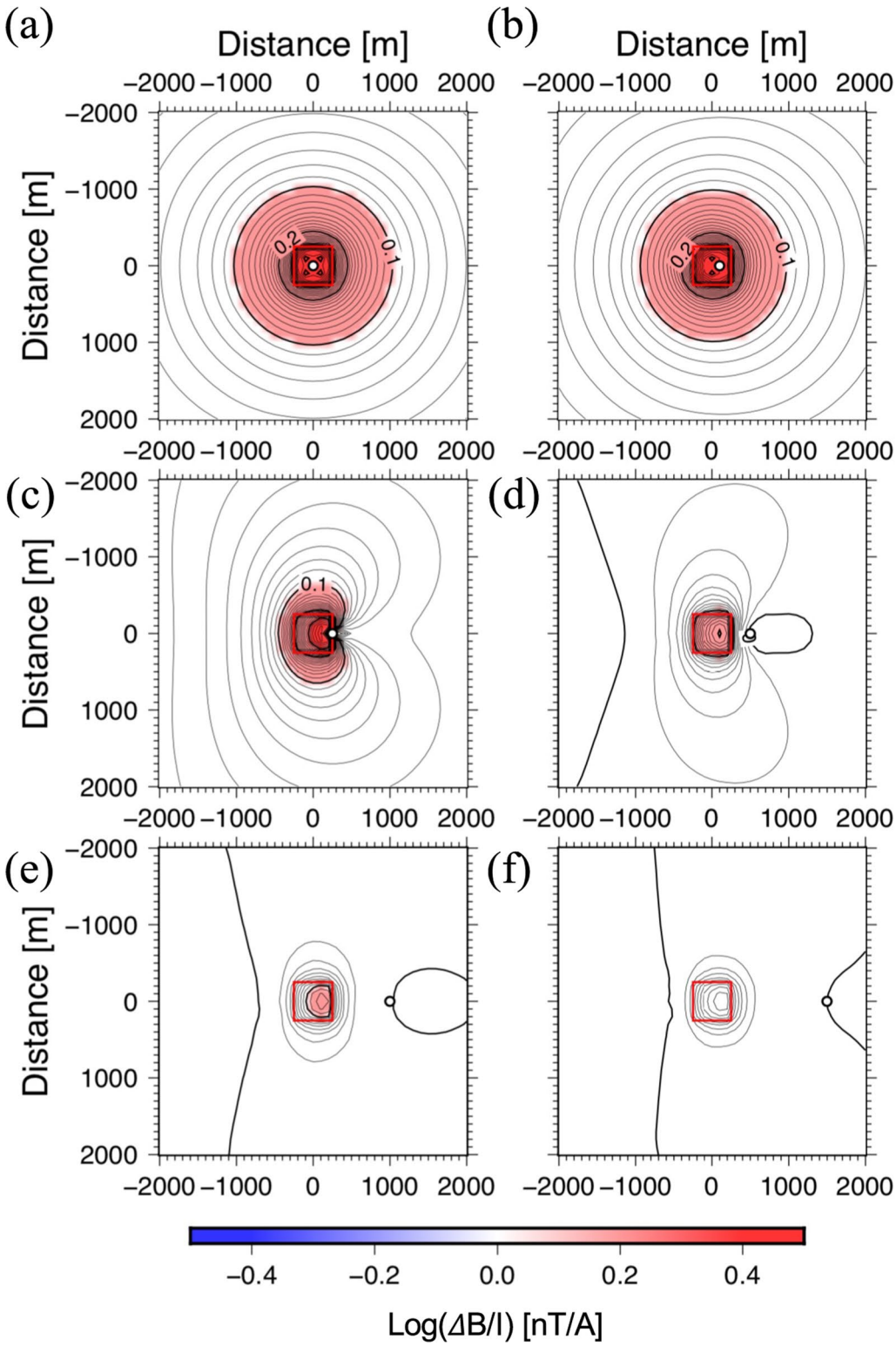

Fig. 10 Type II magnetic field anomaly for the CA model. The open circles indicate the positions of the OBMs. The other conditions are the same as those in Fig. 8. **a** OBM on the center of the anomalous body, (0, 0). **b** OBM on the anomalous body at (100, 0). **c** OBM on the edge of the anomalous body, (250, 0). **d** OBM not on the anomalous body, (500, 0). (**e**) OBM located at (1000, 0). **f** OBM located at (1500, 0)

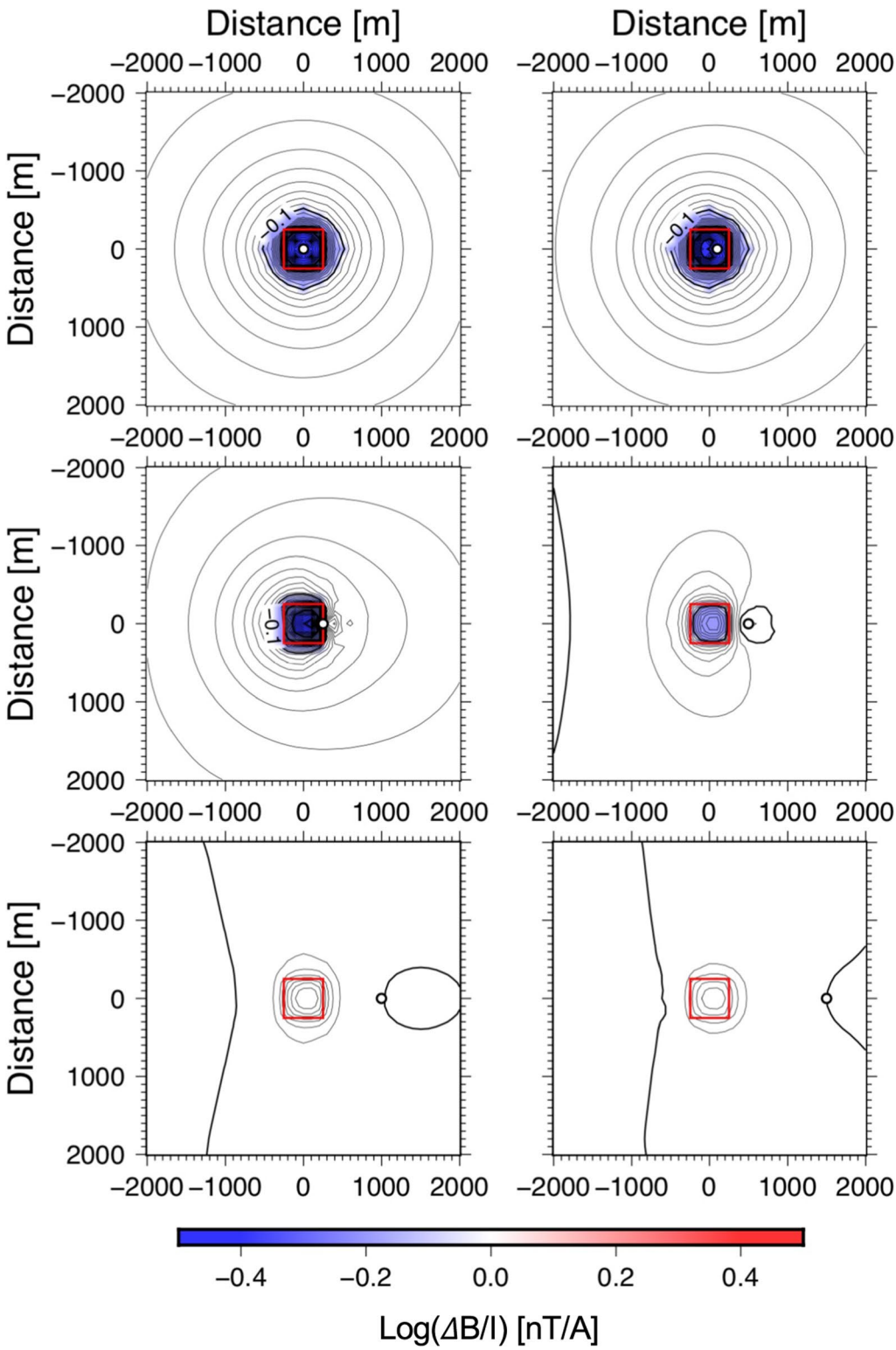

Fig. 11 Type II magnetic field anomaly for the RA model. All conditions except for the electrical resistivity value of the anomalous body are the same as those in Fig. 10

5 Conclusion

In this study, we have developed 3-D forward modeling method for MMR data to estimate the 3-D electrical resistivity structure of shallow oceanic crust. In numerical simulations, singular values arise due to point-sources. However, in this study, we mitigated the impact of singular values by introducing two electrical resistivity models (a background model and the desired 3-D electrical resistivity model) during computation. This enabled us to compensate for the effects of singular values. As a result, we can now simulate how the magnetic field induced by electrical resistivity anomalies within oceanic crust is observed by MMR methods, even in the case of 3-D structures. Our investigation into the relationship between anomalous bodies beneath the seafloor and the induced magnetic field observed by OBMs revealed that lower-resistivity anomalous bodies are more sensitive to exploration using the MMR method than higher-resistivity anomalous bodies compared to the surrounding structures. Furthermore, we demonstrated that increasing the number of locations where electrical current is injected through bipole sources, rather than increasing the number of receivers (OBMs), is effective in exploring anomalous bodies. Supplying electrical current from a ship is more cost-effective and time-efficient than increasing the number of seafloor observation devices. Therefore, enhanced exploration accuracy can be expected through observations with various positions of the bipole source. Moreover, by transforming the developed 3-D forward code into an inversion process, it would be possible to easily estimate the three-dimensional resistivity structure from the acquired data.

Abbreviations

CSEM	Controlled electromagnetic method
MMR	Magnetometric resistivity
OBM	Ocean bottom magnetometer
1-D	One-dimensional
3-D	Three-dimensional
mbsf	m below seafloor
S–R	Source–Receiver
CA	Conductive Anomaly
RA	Resistive Anomaly

Acknowledgements

Figures were produced using GMT software (Wessel et al. 2019; Wessel and Smith 1998). We would like to express our sincere gratitude to Dr. Hiroshi Ichihara for his invaluable discussions of this study. We are also grateful to the editors and the two anonymous reviewers for their insightful comments and suggestions, which significantly improved the manuscript.

Author contributions

NT and MK mainly contributed to the 3-D forward coding. NT contributed to calculations. NS contributed funding to this study. All authors contributed to discussions, and read and approved the final manuscript.

Funding

This research was supported by the special coordination fund for the "Archaean Park Project", and by KAKENHI Grant Numbers 21H01186 from the Japanese Ministry of Education, Culture, Sports, Science and Technology.

Availability of data and materials

Contact the corresponding author to use the 3-D forward code.

Declarations

Ethics approval and consent to participate

Not applicable.

Consent for publication

Not applicable.

Competing interests

The authors declare that they have no competing interests regarding this study.

Author details

[1]Research Institute for Marine Geodynamics, Japan Agency for Marine-Earth Science and Technology, 2-15 Natsushima-cho, Yokosuka 237-0061, Japan. [2]International Research Institute of Disaster Science, Tohoku University, 468-1 Aoba, Aramaki, Aoba-ku, Sendai 980-8572, Japan. [3]Kobe Ocean-Bottom Exploration Center / Department of Planetology, Kobe University, 1-1 Rokkodai, Nada-ku, Kobe 657-8501, Japan.

Received: 2 March 2024 Accepted: 28 August 2024
Published online: 15 October 2024

References

Abderrezak B, Bernard G, Michel A (2017) Down-hole magnetometric resistivity inversion for zinc and lead lenses localization at Tobermalug, county Limerick, Ireland. J Appl Geophys 137:25–33. https://doi.org/10.1016/j.jappgeo.2016.12.010

Becker (1985) Large-scale electrical-resistivity and bulk porosity of the oceanic-crust, deep-sea drilling project hole-504b, Costa-Rica Rift. Initial Rep Deep Sea Drilling Project 83:419–427

Chesley C, Naif S, Key K (2023) Characterizing the porosity structure and gas hydrate distribution at the southern Hikurangi Margin, New Zealand from offshore electromagnetic data. Geophys J Int 234:2411–2428. https://doi.org/10.1093/gji/ggad243

Chen J, Haber E, Oldenburg D (2002) Three-dimensional numerical modelling and inversion of magnetometric resistivity data. Geophys J Int 149:679–697. https://doi.org/10.1046/j.1365-246X.2002.01688.x

Constable S, Weiss C (2006) Mapping thin resistors and hydrocarbons with marine EM methods: insights from 1D modeling. Geophysics 71:G43–G51. https://doi.org/10.1190/1.2187748

Edwards RN, Lee H, Nabighian MN (1978) On theory of magnetometric resistivity (MMR) methods. Geophysics 43:1176–1203. https://doi.org/10.1190/1.1440887

Edwards RN, Law LK, DeLaurier JM (1981) On measuring the electrical conductivity of the oceanic crust by a modified magnetometric resistivity method. J Geophys Res 86(B12):11609–11615. https://doi.org/10.1029/JB086iB12p11609

Edwards RN, Nobes DC, Gomez-Trevino E (1984) Offshore electrical exploration of sedimentary basins: the effects of anisotropy in horizontally isotropic, layered media. Geophysics 49(5):566–576. https://doi.org/10.1190/1.1441691

Edwards RN, Law LK, Wolfgram PA, Nobes DC, Bone MN, Trigg DF, DeLaurier JM (1985) First results of the MOSES experiment: Sea sediment conductivity and thickness determination, Bute Inlet, British Columbia, by magnetometric offshore electrical sounding. Geophysics 50(1):153–161. https://doi.org/10.1190/1.1441825

Evans RL, Webb SC, Jegen M, Sananikone K (1998) Hydrothermal circulation at the Cleft-Vance overlapping spreading center: Results of a magnetometric resistivity survey. J Geophys Res 103(B6):12321–12338. https://doi.org/10.1029/98JB00599

Evans RL, Webb SC (2002) Crustal resistivity structure at 9°50′N on the East Pacific rise: results of an electromagnetic survey. Geopys Res Lett. https://doi.org/10.1029/2001GL014106

Ishizu K, Kasaya T, Goto T, Koike K, Siripunvaraporn W, Iwamoto H, Kawada Y, Ishibashi J (2024) A marine controlled-source electromagnetic application using towed and seafloor-based receivers capable of mapping seafloor and embedded massive sulfides. Geophysics 89:E87–E99. https://doi.org/10.1190/GEO2023-0389.1

Matsuno T, Kimura M, Seama N (2015) Electrical resistivity structure of the snail site at the southern mariana trough spreading center. In: J.-I. Ishibashi et al. (Eds). Subseafloor Biosphere Linked to Hydrothermal Systems: TAIGA Concept, https://doi.org/10.1007/978-4-431-54865-2_19.

Naif S, Key K, Constable S, Evans RL (2015) Water-rich bending faults at the Middle America Trench. Geochem Geophys Geosyst 16:2582–2597. https://doi.org/10.1002/2015GC005927

Naif S, Key K, Constable S, Evans RL (2016) Porosity and fluid budget of a water-rich megathrust revealed with electromagnetic data at the Middle America Trench. Geochem Geophys Geosyst 17:4495–4516. https://doi.org/10.1002/2016GC006556

Nobes DC, Law LK, Edwards RN (1986) The determination of resistivity and porosity of the sediment and fractured basalt layers near the Juan de Fuca Ridge. Geophys J r Astr Soce 86:289–317. https://doi.org/10.1111/j.1365-246X.1986.tb03830.x

Reagan, M.K., Pearce, J.A., Petronotis, K., Almeev, R., Avery, A.A., Carvallo, C., Chapman, T., Christeson, G.L., Ferré, E.C., Godard, M., Heaton, D.E., Kirchenbaur, M., Kurz, W., Kutterolf, S., Li, H.Y., Li, Y., Michibayashi, K., Morgan, S., Nelson, W.R., Prytulak, J., Python, M., Robertson, A.H.F., Ryan, J.G., Sager, W.W., Sakuyama, T., Shervais, J.W., Shimizu, K., and Whattam, S.A. (2015) Site U1439, Proceedings of the International Ocean Discovery Program, https://doi.org/10.14379/iodp.proc.352.103.2015.

Schwalenberg K, Haeckel M, Poort J, Jegen M (2010) Evaluation of gas hydrate deposits in an active seep area using marine controlled source electromagnetics: results from Opouawe Bank, Hikurangi Margin, New Zealand marine. Geology 272:79–88. https://doi.org/10.1016/j.margeo.2009.07.006

Seama N, Tada N, Goto T, Shimoizumi M (2013) A continuously towed vertical bipole source for marine magnetometric resistivity surveying. Earth Planets Space 65:883–891. https://doi.org/10.5047/eps.2013.03.007

Tada N, Seama N, Goto T, Kido M (2005) 1-D resistivity structures of the oceanic crust around the hydrothermal circulation system in the central Mariana Trough using Magnetometric Resistivity method. Earth Planets Space 57:673–677. https://doi.org/10.1186/BF03351846

Tyler RH, Boyer TP, Minami T, Zweng MM, Reagan JR (2017) Electrical conductivity of the global ocean. Earth Planets Space 69:156. https://doi.org/10.1186/s40623-017-0739-7

Védrine S, Bretaudeau F, Darnet M, Hautot S, Tarits P (2023) Exploring geothermal resources using electromagnetic methods in coastal areas of volcanic islands: challenges of nearshore and land 3D controlled-source electromagnetic data. Geophysics. https://doi.org/10.1190/geo2022-0482.1

Wessel P, Luis JF, Uieda L, Scharroo R, Wobbe F, Smith WHF, Tian D (2019) The generic mapping tools version 6. Geochem Geophys Geosyst 20:5556–5564. https://doi.org/10.1029/2019GC008515

Wessel P, Smith WHF (1998) New, improved version of the generic mapping tools released. Eos Trans AGU 79:579. https://doi.org/10.1029/98EO00426

Publisher's Note

Springer Nature remains neutral with regard to jurisdictional claims in published maps and institutional affiliations.